Dynamics of plasma expansion and shockwave formation in femtosecond laser-ablated aluminum plumes in argon gas at atmospheric pressures

Alexander Miloshevsky, Sivanandan S. Harilal, Gennady Miloshevsky,[a)]
and Ahmed Hassanein
Center for Materials Under Extreme Environment, and School of Nuclear Engineering, Purdue University, West Lafayette, Indiana 47907, USA

(Received 24 February 2014; accepted 16 April 2014; published online 29 April 2014)

Plasma expansion with shockwave formation during laser ablation of materials in a background gasses is a complex process. The spatial and temporal evolution of pressure, temperature, density, and velocity fields is needed for its complete understanding. We have studied the expansion of femtosecond (fs) laser-ablated aluminum (Al) plumes in Argon (Ar) gas at 0.5 and 1 atmosphere (atm). The expansion of the plume is investigated experimentally using shadowgraphy and fast-gated imaging. The computational fluid dynamics (CFD) modeling is also carried out. The position of the shock front measured by shadowgraphy and fast-gated imaging is then compared to that obtained from the CFD modeling. The results from the three methods are found to be in good agreement, especially during the initial stage of plasma expansion. The computed time- and space-resolved fields of gas-dynamic parameters have provided valuable insights into the dynamics of plasma expansion and shockwave formation in fs-pulse ablated Al plumes in Ar gas at 0.5 and 1 atm. These results are compared to our previous data on nanosecond (ns) laser ablation of Al [S. S. Harilal *et al.*, Phys. Plasmas **19**, 083504 (2012)]. It is observed that both fs and ns plumes acquire a nearly spherical shape at the end of expansion in Ar gas at 1 atm. However, due to significantly lower pulse energy of the fs laser (5 mJ) compared to pulse energy of the ns laser (100 mJ) used in our studies, the values of pressure, temperature, mass density, and velocity are found to be smaller in the fs laser plume, and their time evolution occurs much faster on the same time scale. The oscillatory shock waves clearly visible in the ns plume are not observed in the internal region of the fs plume. These experimental and computational results provide a quantitative understanding of plasma expansion and shockwave formation in fs-pulse and ns-pulse laser ablated Al plumes in an ambient gas at atmospheric pressures. © *2014 AIP Publishing LLC*. [http://dx.doi.org/10.1063/1.4873701]

I. INTRODUCTION

The laser ablation (LA) and laser-produced plasmas (LPPs) have developed multiple engineering applications over many years.[1–4] Interaction of ultrafast laser beams with materials can be exploited as a source of high-energy radiation such as extreme ultraviolet and X-rays.[5,6] Other potential applications of pulsed LA of materials include micro-machining,[7,8] nanoparticle synthesis,[9,10] polymer fabrication,[11] film growth by pulsed laser deposition,[12–14] and elemental analysis.[15–18] The LPPs are highly transient and dynamic in nature. Therefore, understanding the fundamental physics of the internal structure of plasma plumes and their spatial and temporal evolution during plasma expansion into a background gas at atmospheric pressure is crucial for many engineering applications.

The underlying physical mechanisms of material ablation are different for nanosecond (ns) and femtosecond (fs) laser pulses.[19,20] For laser pulses of the ns duration, the ablation process is governed by heat conduction, melting, evaporation, and plasma formation. The interaction of the ns laser light with the plume can be significant.[21] The plasma that shields the target surface can absorb and scatter the ns laser radiation decreasing the ablation efficiency of materials. An advantage of the fs LA compared to the ablation using the ns lasers is that there is no laser light-plasma interaction during a fs pulse.[22] On the timescale of approximately ~100 fs (ultrashort laser pulse duration), many target atoms are ionized. The electron-ion interaction, lattice relaxation, heat conduction, and hydrodynamic processes occur on much longer timescales on the order of picoseconds.[22] Therefore, the energy of fs laser pulses can be entirely deposited into the target resulting in the efficient ablation. The plasma develops and then expands on the picosecond and nanosecond timescales. It is still a challenge to completely understand the expansion dynamics of the ns and fs plumes in ambient gas. A comparison of the spatial and temporal evolution of ns-pulse and fs-pulse generated plasma could further reveal deeper insights into its expansion dynamics and shockwave structure.

Much experimental and theoretical work has been done to investigate the dynamics and plasma parameters of the ns and fs laser-produced plumes in the presence of ambient gas. The ablation efficiency of the ns laser in contrast to that of the fs laser is found to be significantly higher in a comparative study of metal ablation in air with micro-, nano-, pico-, and femtosecond laser pulses.[22] However, apart from pulse

[a)]Author to whom correspondence should be addressed. Electronic mail: gennady@purdue.edu

duration, the wavelength of laser radiation may affect the ablation efficiency, especially for longer pulses ($\geq$100 ps). Other study demonstrates that under similar laser fluence conditions, the mass ablation is significantly higher for the fs laser compared to that of the ns laser.[23] It is identified in spectroscopic measurements of silicon ablation in air that the electron number density and temperature of fs-pulse plasmas have decreased faster than those of ns-pulse plasmas due to different energy deposition mechanisms.[24] The initial directionality of plasma expansion is also found to be different for the ns and fs LA. The effect of ambient pressure ranging over seven orders of magnitude on the fs laser-generated plasma was studied.[25] The background pressure is found to have a profound effect on the shape, size, and expansion of the plume. The generation of shockwaves in the plume is reported in many studies.[26–29] The primary shock waves which propagate through the ambient gas and secondary shock waves formed in the plume's region were reported in the theoretical study of the temporal and special evolution of the plume expanding into an ambient gas.[14] The internal and external shockwaves in the plume generated by a ns laser pulse in air at 1 atmosphere (atm) are revealed using shadowgraph experiments and gas-dynamic model with radiative heat transfer.[27] The formation of raised spherical rims by shockwaves within a crater on the silicon surface in an ambient air environment ablated by a fs-pulse was observed in an experimental study.[28] Due to the complexity of the LA process, comprehensive experimental and computational methods are required to be used for its studies. To the best of our knowledge, a comparison of plasma expansion and shockwave formation in plumes produced by ns-pulse and fs-pulse lasers in an ambient gas at atmospheric pressure was not reported in details.

We have previously reported an experimental and computational study of the shockwave structure and expansion dynamics of the aluminum (Al) plume generated by a ns-pulse in background Ar at 1 atm performed using shadowgraphy, fast gated self-emission imaging, and computational fluid dynamics (CFD) simulations.[30] It is revealed that the plume produced by a ns laser pulse undergoes an asymmetric expansion on the initial stage with further development of the internal shockwave structure and vortical motion of plasma at later times. The structure of shock waves in the plume during its expansion involves a strong external shock, internal rarefaction shock wave, and many reflected and transmitted shocks. The goal of current work is to investigate the expansion dynamics and internal structure of the plume produced by fs laser pulse using shadowgraphy, fast gated imaging employing intensified CCD (ICCD), and CFD modeling. We consider a particular case when the pulse energy of fs laser ($\sim$5 mJ) is twenty times lower compared to that of the ns laser ($\sim$100 mJ). These energies are typically used for laser-induced breakdown spectroscopy (LIBS) and other analytical approaches.[16,31] The dependence of LIBS results on pulse energies (from 10 to 100 mJ) was analyzed in a recent work.[32] This chemical analysis at the atomic level involving LIBS is very useful in a wide range of fields such as biomedical, industrial, environmental, and space applications.[33,34] Hence, a comparison of hydrodynamics of ns and fs LA plumes with routinely used energies are of great interest. We focus on gas-dynamic aspects of the interaction of fs-pulse produced plume and background Ar gas. Shadowgraphy measures the movement of the shock front. The ICCD fast photography captures the images of hot plasma in the plume during its expansion. The CFD modeling predicts the position of the shock front as well as the gas-dynamic fields of temperature, pressure, density, and velocity. The position of the shock front obtained from three methods is compared. The fields of temperature, pressure, density, and velocity have provided valuable insights into the expansion dynamics of fs laser-ablated Al plumes in background Ar gas at 0.5 and 1 atm. These results for fs ablation of Al are compared to our previous data on LA of Al using ns pulses.[30]

II. EXPERIMENTAL AND MODELING METHODS

A. Experimental setup

Pulses from a Ti-Sapphire laser are used to generate the plasma plume on an Al target. The Ti-Sapphire laser system consists of an oscillator which provided 40 fs FWHM (Full Width at Half Maximum) pulses at $\sim$800 nm. The oscillator pulses are then passed through an amplifier system which is comprised of a stretcher, regenerative, and 4-pass amplifiers and a compressor and finally gives an output of $\sim$10 mJ, 40 fs pulses at $\sim$800 nm. A combination of a half waveplate and a thin film polarizer positioned before the compressor optics is used for attenuating the laser beam. The fs pulses are then focused using f/40 plano-convex lens onto an Al target with a spot size of $\sim$340 μm. For avoiding Ar gas breakdown by the pump pulse, the laser best focal point was positioned behind the target surface. So the use of large spot size (340 μm) avoided the probability of breakdown. The target in the form of flat slab is mounted on a high precision X-Y translation stage to provide fresh target surface for each laser shot, and it is positioned in a vacuum chamber filled with Ar at appropriate pressures. For performing shadowgraphy, a frequency doubled Nd:YAG laser emitting at 532 nm with 4 ns FWHM is used as the probe light. The diameter of the probe beam is 7 mm. Using the probe laser, the expanding plasma plume is imaged onto a CMOS CCD detector using a relay lens. The probe laser energy was controlled using a combination of half wave plate and a cube polarizer and was set at $\sim$3 mJ to avoid air breakdown caused by relay lens focusing. The probe beam was synchronized to the camera and ablation beam using a timing generator, with a maximum temporal jitter of $+/-1$ ns. The delay between the probe and ablation beams was varied to image the plasma plume at different times during its expansion. A narrow band-pass filter with a peak transmission wavelength of 532 nm is used to reject the self-emission from the plasma reaching the detector. For obtaining fast gated images of expanding plasma, an ICCD is used as described in our previous work[30] with a minimum gate width of 2 ns. The images, collected orthogonal to plasma expansion direction, are spectrally integrated in the range of 350–800 nm. The experiment is conducted in a stainless steel vacuum chamber at two different background pressures of $\sim$0.5 and $\sim$1 atm of Ar gas. The laser energy used in this experiment is 5 mJ, which corresponds to a power density $\sim 10^{14}$ W/cm^2.

B. CFD model

The CFD modeling is carried out using the rhoCentralFoam solver provided by the open source OpenFOAM package.[35] The mathematical and algorithmic details of the solver are described in our previous work.[30] Here, we outline the set-up of 2D computational domain and parameters of plasma as appropriate for this study. The model parameters are set within a 2D computational domain with x- and y-dimensions of 1.5 mm and 1.5 mm, respectively. The y-axis is perpendicular to the target surface. A non-uniform 300 × 300 mesh is used with cell sizes of 1 μm in the vicinity of the plasma plume, and the size of mesh increases to 5 μm near the outer boundaries of the computational domain. This mesh set-up allows to resolve the dynamics of plume near a laser-produced crater with a high accuracy. The background is modeled as Ar gas at temperature of ~300 K, mass density of ~1.78 kg/m^3, and two background pressures are used, one ~0.5 atm and another ~1 atm. The laser-induced crater is parameterized with a radius of ~0.17 mm and depth of ~5 μm as it is measured in the experiment. At initial time moment, the crater is filled by Al plasma with a uniform distribution of pressure and temperature fields. The plasma and Ar gas are treated as compressible ideal gases. The initial plasma temperature is set to ~11 605 K as it is estimated in our experiments using optical emission spectroscopy. The initial pressure of the plasma in a crater is ~35 MPa. It is a theoretical estimate that gives the best fit to the experimental position of the shock front at different times. The plasma density derived from a perfect gas law is ~9.8 kg/m^3. The Al plasma and background Ar gas are both motionless (zero velocity) at the initial time.

III. RESULTS AND DISCUSSION

A. Experimental shadowgraphy images of the fs plume

Most of the engineering applications of LA are performed in the presence of an ambient gas leading to the generation of shock waves through the interaction of expanding plume species and ambient gas atoms when the mass of the swept gas is greater than the mass of the ablated plasma. Shadowgraphy is one of the best plasma diagnostic tools to study this shock wave formation and its expansion.[36] Shadowgraphy images correspond to second order of the refractive index field, which reveals inhomogeneities in the medium of interest and, therefore, follows shock wave front position generated by LA plumes. In the present experiment, we used a focused shadowgraphy method[37] to evaluate the fs laser plume expansion, which allows variable magnification of the shadowgram. Fig. 1 displays typical shadowgraphy images representing the expansion of the fs plume in ambient Ar at 1 atm after the onset of plasma for specified times. The x-axis is directed along the target surface. The y-axis is normal to the target. The expansion is symmetric relative to normal (symmetry y-axis) to the target surface. The similar images were also produced for the fs plume expanding in Ar gas at 0.5 atm (not shown).

At t ~ 100 ns, the front boundary of the plasma plume is well defined. However, at later times, the change of refractive index at plume-ambient boundary becomes weaker. At t ~ 1000 ns, the boundary requires a close examination to be identified. At the center of each plume shown in Fig. 1, the ejected material is observed representing the location where the laser beam has interacted with the Al target.

B. Experimental ICCD images of the fs plume

Photography of the plume's self-emission employing fast gated ICCD provides two-dimensional snapshots of three-dimensional plume expansion. Fig. 2 shows the ICCD images of the expanding plume measured at various times for 1 atm and 0.5 atm of background Ar gas. All images are spectrally integrated and obtained with a gate width of 2 ns. For 1 atm, the interface between the plume and ambient is sharp until t ~ 175 ns, and it breaks down for later times. The plumes captured by ICCD imaging maintain nearly symmetric shapes for all times. The hottest parts of the plume corresponding to a region of intense radiation are marked by

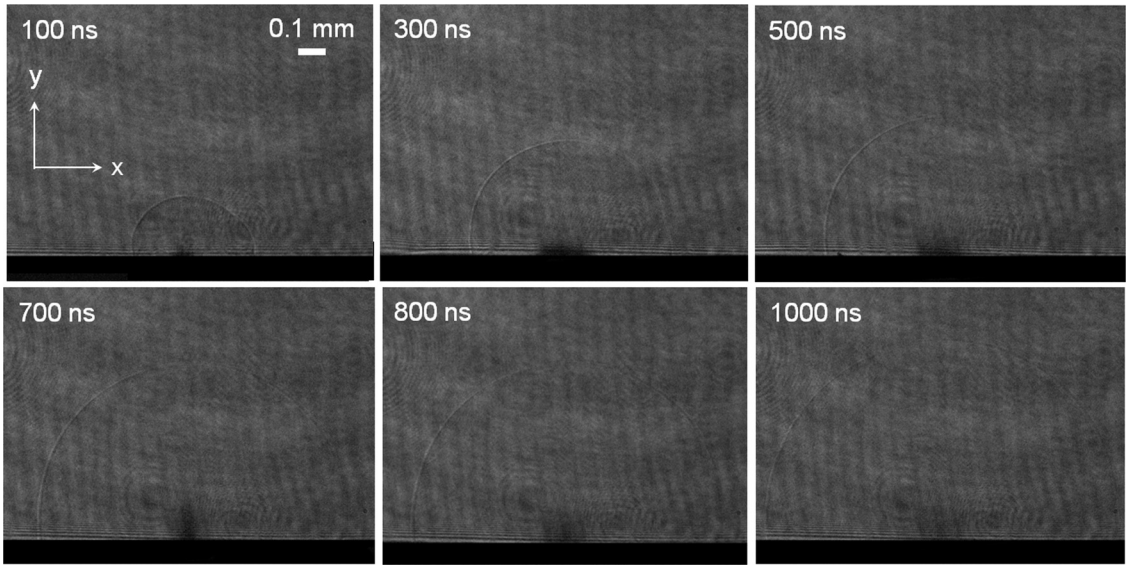

FIG. 1. Shadowgraphy images representing the expansion of the fs-pulse generated plume in ambient Ar at 1 atm after the onset of plasma for specified times.

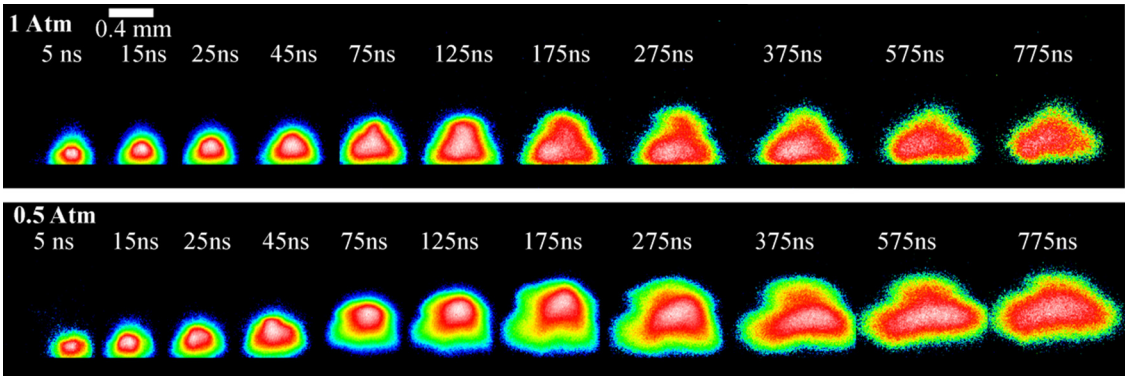

FIG. 2. The ICCD images of fs plumes in Ar gas at 1 atm and 0.5 atm for various times after the onset of plasma formation. All images were obtained with a gating time of 2 ns. Each image is normalized to its peak intensity for better clarity.

white and red colors. The peripheral regions colored in green and blue are more cold. Rising expansion of plasma is observable between $t \sim 5$ ns and $t \sim 175$ ns, and then it ceases for later times. The plume boundary sharpness of the image drops between $t \sim 275$ ns and $t \sim 775$ ns, since the intensity of the radiation decreases because of plume cooling. For 0.5 atm, the length scale of plasma expansion is found to be greater, and the plasma does not cool rapidly compared to that at 1 atm. A faint white region is still visible at $t \sim 775$ ns. Therefore, the center of the plume is hotter at this time moment for 0.5 atm compared to that for 1 atm.

C. Computational profiles of gas-dynamic parameters in the fs plume

During the LA process of Al, a crater with high-density plasma is formed. The dense plume expands, then, above the target surface pushing the ambient Ar gas away. The computational y-profiles of temperature, pressure, density, and y-component of velocity in the fs laser-ablated Al plume expanding in background Ar gas at 1 atm are shown in Fig. 3 for various time moments. In Fig. 3(a), we analyze the temporal behavior of temperature in the plume during its expansion. First, let us focus on the plume's center. During the first $t \sim 50$ ns, the plume expands less than ~ 0.1 mm. A nearly stepwise temperature drop from $\sim 11\,605$ K to ~ 2500 K of the plasma is occurred.

This initial temperature decrease is due to the intense heat transfer that exists between the hot plasma and cold Ar gas. In a time window ranging from $t \sim 50$ ns to $t \sim 250$ ns, the plasma near the plume's center cools further to <1500 K. At later times (until $t \sim 2000$ ns), the temperature undergoes only small variations about ~ 1400 K meaning that the heat exchange between the hot plasma near the plume's center and background Ar gas becomes negligible. This is also confirmed by observation that the temperature drops to background temperature ~ 300 K within a distance ~ 0.4 mm (at $t \sim 1000$ ns and $t \sim 2000$ ns), while the plume expands up to ~ 1.2 mm (Fig. 3(a)). The hot high-temperature region in the vicinity of the plume's center at later expansion stages was previously reported.[14] Second, let us consider the behavior of temperature at the shock front. From $t \sim 50$ ns to $t \sim 250$ ns, the temperature of the plume's front drops from ~ 2000 K to ~ 800 K. At $t \sim 500$ ns, the temperature decreases further to ~ 500 K. At this time moment, the temperature is slightly reduced behind the shock front. This fast cooling of the plume is due to mixing with the ambient Ar gas. From $t \sim 1000$ ns to $t \sim 2000$ ns, a cold region with background temperature ~ 300 K forms between the plume's center and its shock front. However, the temperature of the plume's center remains much higher compared to that at the shock front (Fig. 3(a)).

The expansion of dense high-pressure LPP in background Ar gas at 1 atm generates strong shocks at the interface between plasma and Ar gas. During the initial stage of expansion, the plume impacts the ambient Ar gas as a supersonic piston.[14] It is seen in Fig. 3(b) that at $t \sim 50$ ns, the pressure is ~ 0.4 MPa at the plume's center, a large drop from the initial pressure of ~ 35 MPa in the crater. The shock front is formed with pressure ~ 2.5 MPa much greater than that in the region behind or before it. In a time window ranging from $t \sim 50$ ns to $t \sim 500$ ns, the pressure at the plume's center decreases further to background pressure ~ 0.1 MPa. During this time interval, the pressure at the shockwave front also drops to ~ 0.3 MPa. The expansion slows down due to the greater counteraction of the ambient gas. At $t \sim 1000$ ns and $t \sim 2000$ ns, the pressure is below background Ar pressure in the central region within a distance of ~ 0.35 mm and ~ 0.8 mm, respectively (Fig. 3(b)). The pressure at the shock front experiences a small change. Shadowgrams (Fig. 1) also showed weak pressure variation at the plume-ambient interface at these times. At $t \sim 2000$ ns, the pressure is slightly below ~ 0.2 MPa. The shock front propagates ~ 0.7 mm during the first 1000 ns and about ~ 0.5 mm during the next 1000 ns. A comparison between the temperature and pressure profiles in Figs. 3(a) and 3(b) shows an agreement in the location of temperature and pressure fronts until $t \sim 250$ ns. For later times, the peak of temperature lags behind the peak of pressure.

The LPP with the initial mass density ~ 9.8 kg/m^3 expands rapidly outwards from the crater. The shock front pushes into the stationary Ar gas causing its compression to high density in a thin region. As a result, a large jump of mass density is observed at the shock front with a low-density region formed behind it (Fig. 3(c)). At $t \sim 50$ ns, the mass density of plasma near the plume's center is already ~ 1 kg/m^3, lower than background Ar density of ~ 1.7 kg/m^3. During this short time interval, the mass density at the shock front drops below ~ 5 kg/m^3. From $t \sim 50$ ns to $t \sim 250$ ns, the mass density of plasma near the plume's center decreases further, and then it remains

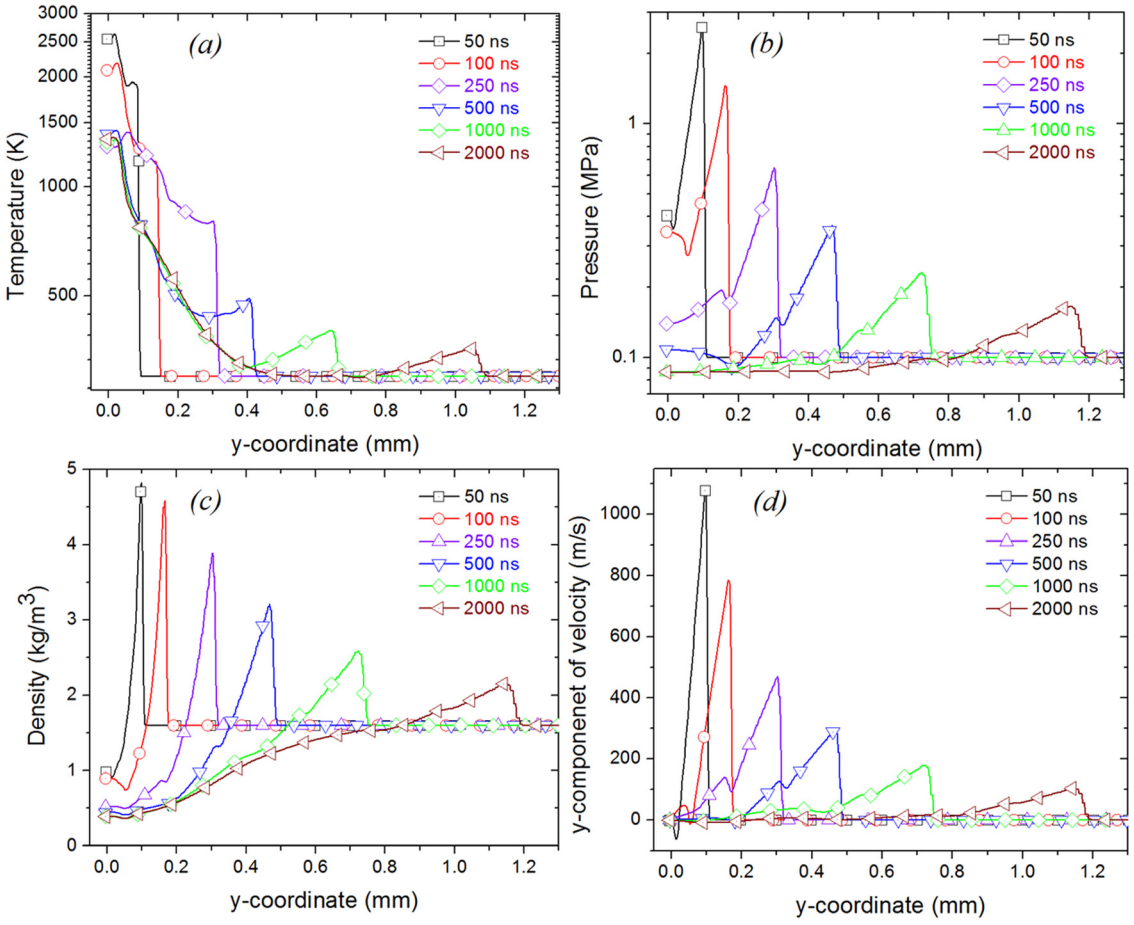

FIG. 3. The computational profiles of (a) temperature, (b) pressure, (c) mass density, and (d) y-component of velocity along the y-coordinate (symmetry axis) at position x = 0 for various times. Profiles are plotted for the fs laser-ablated Al plume expanding in background Ar at 1 atm.

constant for later times. It is seen in Fig. 3(c) that the mass density at the plume's center is lower by ~1.2 kg/m^3 compared to background Ar density. At t ~ 2000 ns, the mass density at the shock front is reduced to ~ 2.25 kg/m^3.

The expansion of the plasma plume is achieved due to transformation of thermal energy into kinetic energy with resultant drop in temperature and pressure. Consequently, the plume's front of the expanding plasma acquires a supersonic velocity in a very short time. The y-components of velocity are shown in Fig. 3(d) for various times. At t ~ 50 ns, the velocity of the shock front is ~1100 m/s. This is more than three times higher compared to the speed of sound in background Ar gas at room temperature, ~320 m/s. The shock wave then experiences a rapid deceleration between t ~ 50 ns and t ~ 500 ns. At t ~ 500 ns, the velocity is ~300 m/s, that is, below the sound speed in Ar gas. At later times, the shock front does not decelerate at the same rate. In a time window from t ~ 500 ns to t ~ 2000 ns, the velocity is slowly reduced below ~200 m/s. The motion of plasma behind the shock is insignificant since the y-component of velocity is close to ~0 m/s (Fig. 3(d)).

D. Computational pressure and velocity fields in the fs plume

A computational contour plot of the pressure field in Ar gas at 1 atm is shown in Fig. 4 (Multimedia view) for various times. At t ~ 100 ns, the fs plume has expanded slightly more, ~2.1 mm, in the x-direction than it is moved in the y-direction, ~1.9 mm. This is because the initial radius of a plasma spot is larger than the depth of a crater (see Sec. II). There is a much greater increase of pressure at the shock front along the y-direction than that in the x-direction. The plume expansion is forward directed. The pressure within the plume is several times greater than background Ar pressure of 0.1 MPa. At t ~ 500 ns, the plume has advanced about ~0.49 mm in the y-direction and about ~0.41 mm in the x-direction. Thus, the shock front of the fs plume has traveled more ~0.8 mm in the y-direction. The pressure still remains higher along the y-direction. However, the pressure in the x-direction has also increased.

A region with pressure ~0.09 MPa that is lower than background Ar pressure has developed at the plume's center. At t ~ 1000 ns, the plume has expanded up to ~0.75 mm along the y-direction and up to ~0.62 mm along the x-direction. At the shock front, pressure remains slightly higher along the y-direction, but pressure along the x-direction is also significantly increased. The magnitude of pressure at the plume's front becomes more uniform. At the plume's center within a radius of ~0.4 mm, the pressure has dropped to ~0.086 MPa. At t ~ 2000 ns, the fs plume has progressed up to ~1.18 mm in the y-direction and up to ~1.05 mm in the x-direction. A uniform pressure is

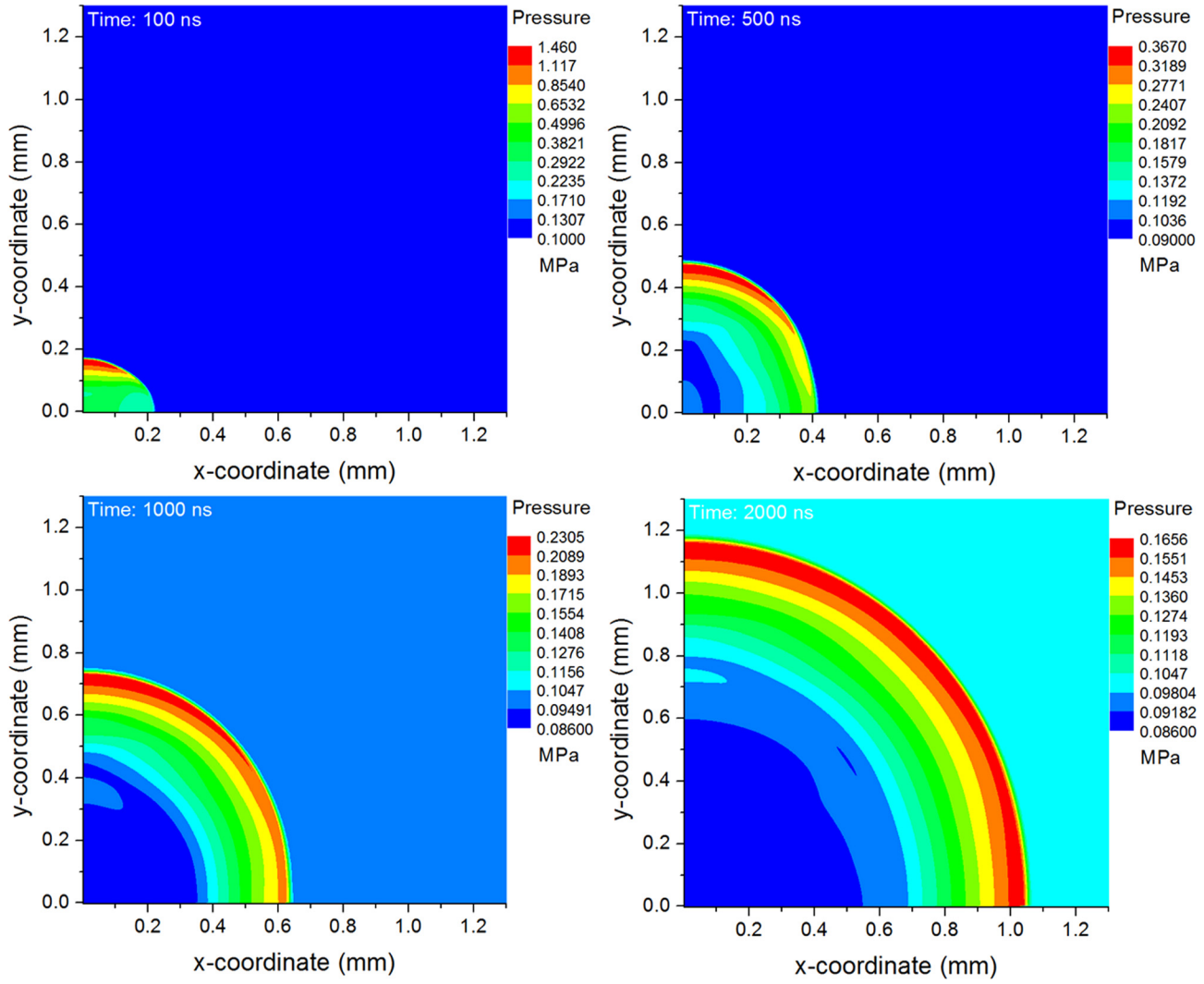

FIG. 4. Computational contour plot of the pressure field in the fs-pulse generated plume expanding in Ar gas at 1 atm for various time moments. (Multimedia view) [URL: http://dx.doi.org/10.1063/1.4873701.1]

developed on the entire shock front. At the plume's center, the pressure remains lower than background Ar pressure. The region of low pressure has increased up to ~0.6 mm.

The computational vector field of velocity in the fs plume expanding in Ar gas at 0.5 atm is shown in Fig. 5 for various times.

At $t \sim 100$ ns, the volume of plasma-argon gas involved in the intensive motion is localized within a radius of ~0.2 mm from the plume's center. It is seen in Fig. 5 that the flow of plasma is directed outwards from a crater. The velocity is small in the vicinity of the plume's center. At the shock front, the plasma velocity in the y-direction is much higher than that in the x-direction. On this stage of expansion, the velocity is angle-dependent. The background Ar gas becomes also involved in the chaotic motion (blue arrows). At $t \sim 500$ ns, the plasma velocity at the shock front is still higher in the y-direction. In the vicinity of the plume's center, the vortex starts to develop. At $t \sim 1000$ ns, the shock front of the fs plume continues to have a higher velocity in the y-direction. However, the difference in the magnitude of velocities decreases along the y- and x-direction. The field of velocity is non-uniform within the vortex region. At $t \sim 2000$ ns, the plume's shape is asymmetric with larger expansion in the y-direction. The velocity becomes uniformly distributed along the entire shock front. The outward-directed speed of plasma is lower behind the shock front. The vortex is completely formed at the plume's center. The speed of flow within the vortex region is considerably increased. At the front of this vortex, there is another small vortex with the center at $x \sim 0.4$ mm and $y \sim 0.4$ mm.

E. Comparison of shock front position in the fs plume

A comparison of the y-position of the shock front in the fs plume expanding in Ar gas obtained from shadowgraphy, ICCD imaging, and CFD modeling is demonstrated in Fig. 6(a) for 1 atm and in Fig. 6(b) for 0.5 atm, respectively. For $t < 400$ ns, the y-position of plume front in Ar gas at 1 atm determined from three methods is in rather good agreement (Fig. 6(a)). There is only small discrepancy between the measured and calculated profiles. The ICCD's plume front estimate is not accurate after $t \sim 400$ ns. The fast gated images of the plasma are found to cease at times ~>400 ns, while the plume-ambient interface observed in shadowgram

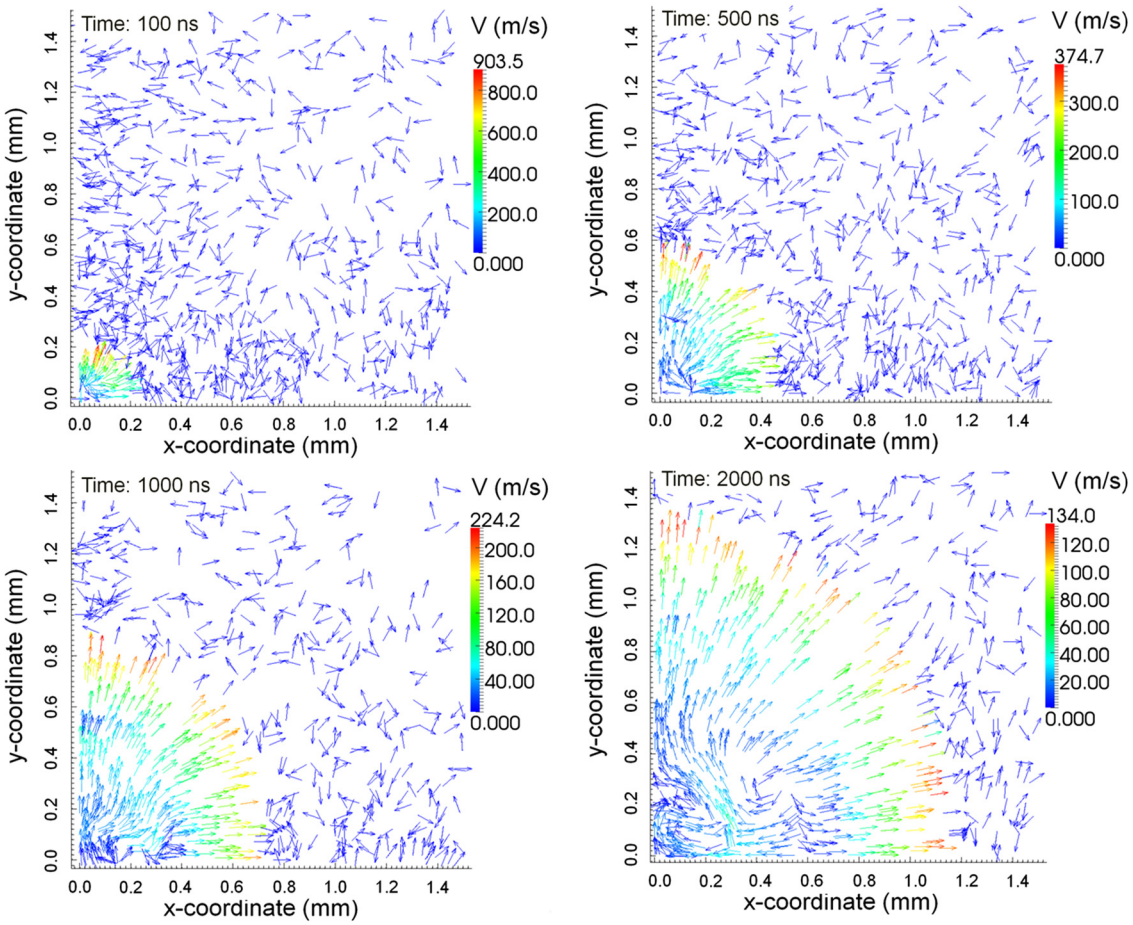

FIG. 5. The computational vector field of velocity in the fs-pulse produced plume expanding in Ar gas at 0.5 atm for various time moments.

is continuously propagating at larger distances away from the target. This indicates that the major emission from the plasma is due to target bulk atoms/ions, while the plume-ambient boundary is not generating any visible emission except the refractive changes in the medium. Also, in the beginning of plume generation and expansion, ICCD profiles showed faster expansion. This could be caused by extreme brightness of the plasma at the earlier times as well as ambient gas excitation and ionization. The shadowgraphy and computational results show a good agreement until $t \sim 1500$ ns. Shadowgraphy profile becomes inaccurate at later times because of poor image resolution creating the difficulty of measuring the y-position of a shock front.

Similarly, the y-position of the shock front in Ar gas at 0.5 atm obtained from shadowgraphy, visible images, and CFD modeling compares well until $t \sim 500$ ns (Fig. 6(b)), although the discrepancy between curves is larger than in the case of plume expansion in Ar gas at 1 atm. It is seen that the position of the shock front predicted by the ICCD method is more advanced than that obtained from the shadowgraphy approach. The CFD profile lags behind the shadowgraphy profile to a greater extent than the same profile shown in Fig. 6(a). After $t \sim 500$ ns, the ICCD method becomes again inaccurate. The results from shadowgraphy and CFD modeling continue to be in good agreement throughout the time considered. During the first 200 ns, the plasma plume expands very rapidly in Ar gas at 1 atm and 0.5 atm, and it begins to decelerate afterwards. At $t \sim 2000$ ns, the y-position of the shock front is only advanced forward by $\sim$0.12 mm in Ar gas at 0.5 atm compared to that in Ar gas at 1 atm (computational curves in Figs. 6(a) and 6(b)).

F. Comparison between the ns and fs laser-ablated Al plumes

In our previous work, the ns LA of Al was studied in details.[30] It is interesting to identify similarities and differences between the ns and fs laser-ablated Al plumes. However, due to the difference in pulse duration of approximately five orders of magnitude between typical ns and fs laser systems, comparative LA studies using similar laser power densities are difficult. For analytical applications, the power density for fs lasers is typically in the range of $\sim 10^{13}$–10^{14} W/cm^2, while for ns lasers, this is often in the range of $\sim 10^{9}$–10^{10} W/cm^2. For the present comparison, we used laser intensities of 8×10^9 W/cm^2 (100 mJ/pulse) and 1×10^{14} W/cm^2 (5 mJ/pulse) for the ns and fs LA, respectively. For reader's convenience, we adapt Fig. 8 from our previous work[30] in Fig. 7 and compare those gas-dynamic profiles with results shown in Fig. 3.

During $t \sim 2000$ ns, the ns laser-ablated Al plume expands $\sim$3.5 mm (Fig. 7) that is almost three times larger than the expansion of the fs laser-ablated Al plume, $\sim$1.2 mm (Fig. 3). This greater expansion of the ns plume can be attributed to longer pulse duration and higher pulse

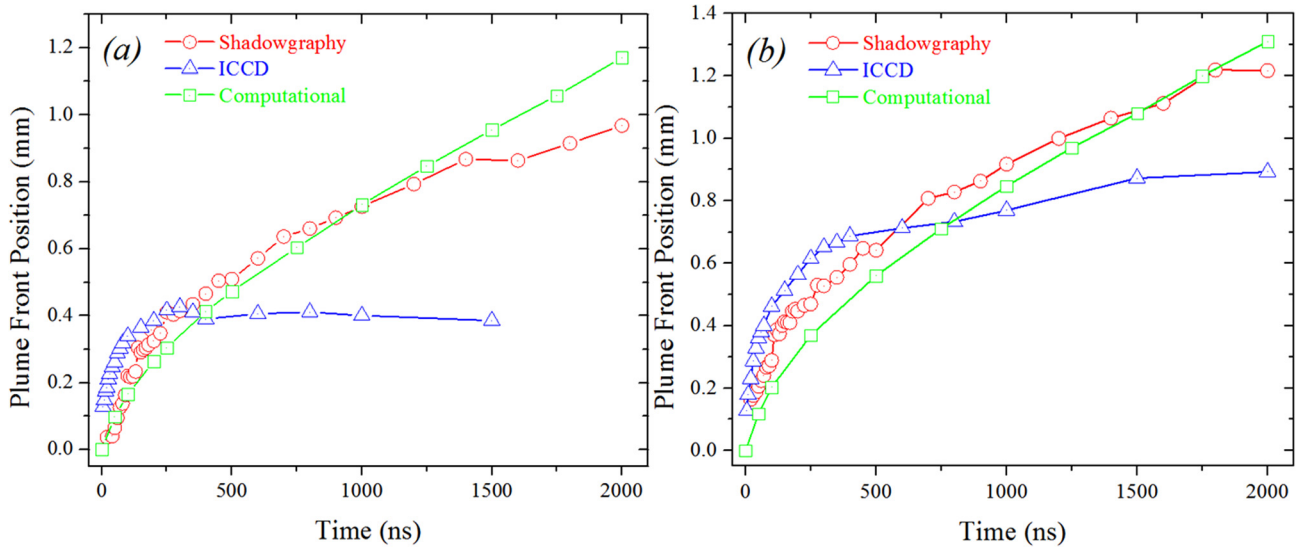

FIG. 6. Comparison of the y-position of the shock front in the fs-pulse generated plume expanded in Ar gas at (a) 1 atm and (b) 0.5 atm. The profiles are derived from shadowgraphy, ICCD images, and CFD modeling.

energy of the ns laser. The cooling of the ns plume (Fig. 7(a)) during the simulated time of 2000 ns is roughly similar to that of the fs plume (Fig. 3(a)) during the first 250 ns. The temperature decreases almost linearly with the distance from the plume's center to its outermost boundary. There is an abrupt drop of temperature at the shock front to background temperature. The temperature range and fine details in profiles are, however, different for the ns and fs plumes. After $t \sim 250$ ns, the fs plume cools down further demonstrating a hot central region with time-independent temperature gradient ($t \sim 500$ ns, $t \sim 1000$ ns, and $t \sim 2000$ ns), an intermediate region with background temperature ~ 300 K ($t \sim 2000$ ns),

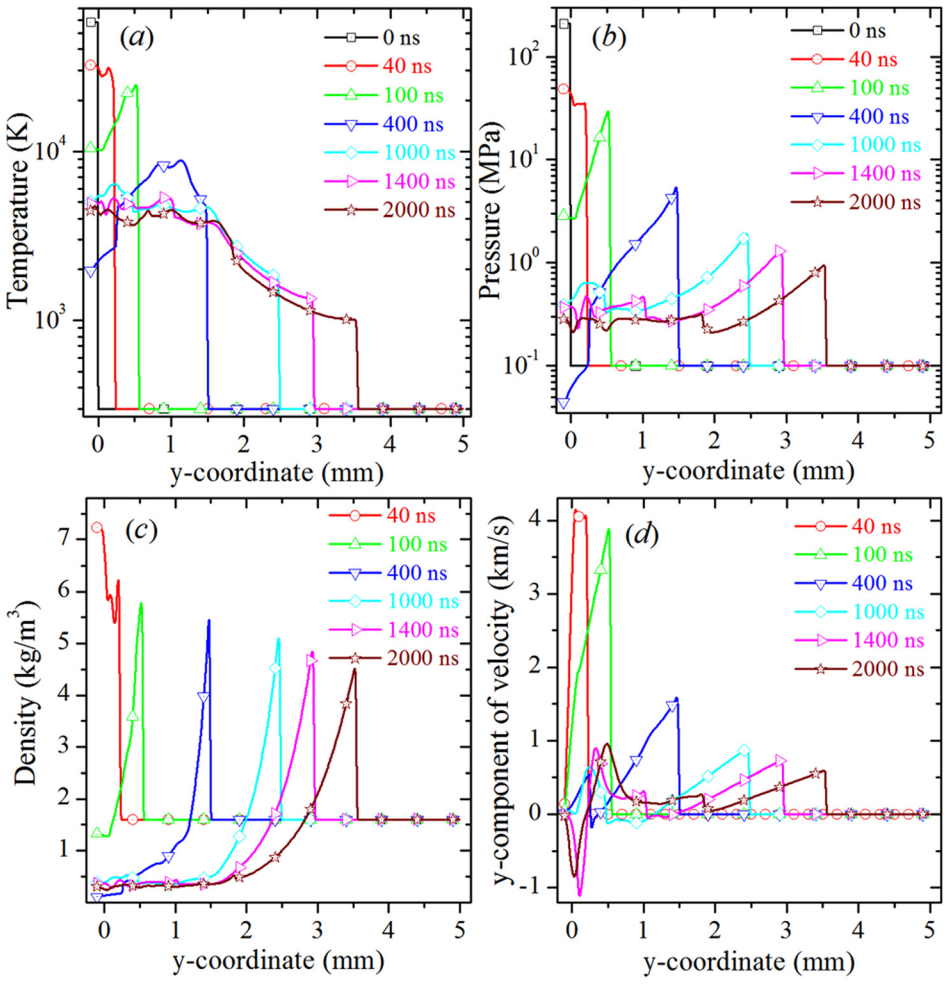

FIG. 7. The computational profiles of (a) temperature, (b) pressure, (c) mass density, and (d) y-component of velocity along the y-coordinate (symmetry axis) at position $x = 0$ for various times. Profiles are plotted for the ns laser-ablated Al plume expanding in background Ar at 1 atm. The figure is adapted from our previous work.[30]

and a plume front with a small jump in temperature ($t \sim 1000$ ns and $t \sim 2000$ ns) (Fig. 3(a)). A faster decrease of temperature in the fs plume compared to that in the ns plume was also reported in an experimental study.[24]

The initial pressure ~35 MPa in the fs plume is six times lower than that in the ns plume, ~210 MPa.[30] This could be related to lower laser energy used for fs-pulse ablation compared to ns-pulse ablation in the present study. Therefore, the internal structure of shock and rarefaction waves characteristic for the ns plume (Fig. 7(b)) is not observed in the fs plume (Fig. 3(b)). The secondary shocks are also not seen in the shadowgraphy images (Fig. 1). After $t \sim 1000$ ns, the pressure behind the shock front in the ns plume fluctuates around ~0.3 MPa that is greater than background Ar pressure of 0.1 MPa. In contrast, the pressure drops below background Ar pressure in the central region of the fs plume after ~1000 ns (Fig. 3(b)).

The overall behavior and shape of mass density profiles at various times are very similar. In both ns and fs plumes, the mass density undergoes a large jump at the shock front with a low-density region formed behind it. In the vicinity of the plume's center, the mass density becomes lower than background Ar density. However, at the end of expansion ($t \sim 2000$ ns), the mass density is about two times lower at the shock front in the fs plume (Fig. 3(c)) compared to that in the ns plume (Fig. 7(c)). At this time moment, the density front is also much broader in the fs plume.

The initial magnitude of velocity in the ns plume (Fig. 7(d)) is higher about four times than that in the fs plume (Fig. 3(d)). At $t \sim 2000$ ns, the velocity of the shock front drops to ~500 m/s (above the sound speed in Ar gas) in the ns plume, while the front velocity is ~100 m/s (below the sound speed in Ar gas) in the fs plume. The development of oscillating velocity profiles in the fs plume near its center is not observed unlike those seen in the ns plume. Instead, at later times (>500 ns), the velocity is close to zero in the internal region of the fs plume (Fig. 3(d)).

IV. CONCLUSIONS

The expansion of Al plumes produced by fs-pulse laser in Ar gas at 0.5 and 1 atm is studied using shadowgraphy, ICCD imaging, and CFD modeling. The spatial and temporal evolution of temperature, pressure, density, and y-component of velocity in an expanding plume is analyzed. The following features in the expansion dynamics of the fs plume are revealed. During the initial stage of expansion, the plasma cools down rapidly. At later times, hot (~1400 K), cold (~300 K), and warm (>300 K) gases (plasma) develop in the central, intermediate, and peripheral regions of the expanded plume. The pressure experiences a large discontinuous jump at the shock front with further development of a rarefaction region behind it, where, at late times, the pressure is less than background Ar pressure. At early times, the shock-front pressure is much higher in the direction perpendicular to the target surface. But later, the pressure becomes uniformly distributed over the entire shock front. The internal shockwave structure is not found in the fs plume during its expansion. A large jump of mass density is observed in a thin layer at the shock front. Behind the shock, the rarefaction wave with mass density much lower than background Ar density develops on a time scale less than tens of nanoseconds. The shock front initially propagates at a supersonic speed relative to background Ar gas until its velocity becomes subsonic at late times. The magnitude of velocity that is initially much greater in the direction perpendicular to the target surface turns out later to be uniform along the shock front. A peak value of velocity at the shock front decays smoothly to zero velocity at the plume's center. At late times, the vortical motion is developed in the rarefaction region. The expansion is affected by background Ar pressure, since the fs plume expands further about ~0.12 mm in Ar gas at 0.5 atm. The modeling results on the position of the shock front in background Ar gas at 0.5 atm and 1 atm are found in rather good agreement with the experimental data. CFD simulations in quantitative detail reproduce the location of the shock.

The results of the fs LA of Al are compared to those from our previous work on the ns LA of Al. This comparison is of particular interest since it reveals similarities and differences in the expansion dynamics of ns-pulse and fs-pulse produced plumes. In our studies, the ns-pulse energy was twenty times higher than the pulse energy of the fs laser. The overall shape of the fs and ns plumes is found to be very similar during their expansion in Ar gas at 1 atm. In both cases, the plume acquires a nearly spherical shape at the end of expansion. This is because the interaction of the expanding plasma with background Ar gas crucially decelerates its expansion in the forward direction. The ablation process is considerably influenced by the pulse duration of the used laser source as well as the laser pulse energy. During $t \sim 2000$ ns, the ns laser-produced plume is expanded three times larger compared to that generated by the fs laser. This can be explained by noting that the deposited energy during a longer ns pulse is many times higher than the fs pulse energy. Thus, in our study, the ablation efficiency of the fs laser is significantly lower. The magnitudes of pressure, temperature, mass density, and velocity are found to be lower in the fs laser-produced plume in the studied laser intensity range. The dynamics and values of these parameters in the fs plume develop and attenuate more quickly on the same timescale compared to those of the ns plume. The mass density, temperature, pressure, and velocity in the fs plume are significantly more evolved during $t \sim 2000$ ns. The oscillatory shock waves are not observed in the internal region of the fs plume, while these shock waves are clearly visible in the ns plume. The oscillatory-free or oscillatory regime of the plume can be important in particular engineering applications of pulsed LA of materials.

ACKNOWLEDGMENTS

This work was partially supported by the US DOE, Office of the NNSA (Award No. DE-NA0001174). The authors thank Dr. Prasoon Diwakar, Nazar Farid, and Nicole LaHaye for help with experiments.

[1]D. Bauerle, *Laser Processing and Chemistry* (Springer Verlag, Berlin, 2011).

[2]D. B. Chrisey and G. K. Hubler, *Pulsed Laser Deposition of Thin Films* (Wiley, New York, 1994).
[3]J. C. Miller and R. F. Haglund, *Laser Ablation and Desorption* (Academic Press, New York, 1998).
[4]S. C. Singh, H. B. Zeng, C. Guo, and W. Cai, *Nanomaterials: Processing and Characterization with Lasers* (Wiley-VCH, 2012).
[5]C. Chenais-Popovics, O. Rancu, P. Renaudin, and J. C. Gauthier, Phys. Scr. **T65**, 163–167 (1996).
[6]S. S. Harilal, R. W. Coons, P. Hough, and A. Hassanein, Appl. Phys. Lett. **95**(22), 221501 (2009).
[7]C. Momma, S. Nolte, B. N. Chichkov, F. vonAlvensleben, and A. Tunnermann, Appl. Surf. Sci. **109–110**, 15–19 (1997).
[8]S. V. Garnov, V. I. Konov, T. Kononenko, V. P. Pashinin, and M. N. Sinyavsky, Laser Phys. **14**(6), 910–915 (2004).
[9]B. Kumar and R. K. Thareja, Phys. Plasmas **20**(5), 053503 (2013).
[10]S. S. Harilal, N. Farid, A. Hassanein, and V. M. Kozhevin, J. Appl. Phys. **114**(20), 203302 (2013).
[11]C. R. Phipps, *Laser Ablation and Its Applications* (Springer, New York, 2007).
[12]D. B. Geohegan, Appl. Phys. Lett. **60**(22), 2732–2734 (1992).
[13]R. Castro-Rodriguez, D. R. Coronado, A. Iribarren, B. E. Watts, F. Leccabue, and J. L. Pena, Appl. Phys. A **81**(7), 1503–1507 (2005).
[14]A. V. Bulgakov and N. M. Bulgakova, J. Phys. D: Appl. Phys. **28**(8), 1710–1718 (1995).
[15]E. Tognoni, V. Palleschi, M. Corsi, and G. Cristoforetti, Spectrochim. Acta, Part B **57**(7), 1115–1130 (2002).
[16]D. W. Hahn and N. Omenetto, Appl. Spectrosc. **64**(12), 335a–366a (2010).
[17]D. W. Hahn and N. Omenetto, Appl. Spectrosc. **66**(4), 347–419 (2012).
[18]K. Stelmaszczyk, P. Rohwetter, G. Mejean, J. Yu, E. Salmon, J. Kasparian, R. Ackermann, J. P. Wolf, and L. Woste, Appl. Phys. Lett. **85**(18), 3977–3979 (2004).
[19]M. R. Kasaai, V. Kacham, F. Theberge, and S. L. Chin, J. Non-Cryst. Solids **319**(1–2), 129–135 (2003).
[20]V. I. Mazhukin, A. V. Mazhukin, and M. G. Lobok, Laser Phys. **19**(5), 1169–1178 (2009).
[21]V. Margetic, A. Pakulev, A. Stockhaus, M. Bolshov, K. Niemax, and R. Hergenroder, Spectrochim. Acta, Part B **55**(11), 1771–1785 (2000).
[22]K. H. Leitz, B. Redlingshofer, Y. Reg, A. Otto, and M. Schmidt, Phys. Procedia **12**, 230–238 (2011).
[23]B. Verhoff, S. S. Harilal, and A. Hassanein, J. Appl. Phys. **111**(12), 123304 (2012).
[24]X. Zeng, X. L. Mao, R. Greif, and R. E. Russo, Appl. Phys. A **80**(2), 237–241 (2005).
[25]N. Farid, S. S. Harilal, H. Ding, and A. Hassanein, Appl. Phys. Lett. **103**(19), 191112 (2013).
[26]P. Yeates and E. T. Kennedy, J. Appl. Phys. **108**(9), 093306 (2010).
[27]S. B. Wen, X. L. Mao, C. Y. Liu, R. Greif, and R. Russo, J. Phys.: Conf. Ser. **59**, 343–347 (2007).
[28]S. Panchatsharam, B. Tan, and K. Venkatakrishnan, J. Appl. Phys. **105**(9), 093103 (2009).
[29]P. Yeates and E. T. Kennedy, Phys. Plasmas **18**(6), 063106 (2011).
[30]S. S. Harilal, G. V. Miloshevsky, P. K. Diwakar, N. L. LaHaye, and A. Hassanein, Phys. Plasmas **19**(8), 083504 (2012).
[31]S. S. Harilal, P. K. Diwakar, and A. Hassanein, Appl. Phys. Lett. **103**(4), 041102 (2013).
[32]L. Kurek, M. L. Najarian, D. A. Cremers, and R. C. Chinni, J. Visualized Exp. **e50876**(79), 1 (2013).
[33]B. Kearton and Y. Mattley, Nat. Photonics **2**, 537–540 (2008).
[34]R. Gaudiuso, M. Dell'Aglio, O. De Pascale, G. S. Senesi, and A. De Giacomo, Sensors **10**(8), 7434–7468 (2010).
[35]See http://www.openfoam.com for OpenFOAM, User Guide, Version 2.2.2, 2014.
[36]R. W. Schoenlein, J. G. Fujimoto, G. L. Eesley, and T. W. Capehart, Phys. Rev. Lett. **61**(22), 2596–2599 (1988).
[37]G. S. Settles, *Schlieren and Shadowgraph Techniques*. (Springer Verlag, Berlin, Germany, 2006).